Journal of Environmental Chemical Engineering 14 (2026) 123587

Contents lists available at ScienceDirect

Journal of Environmental Chemical Engineering

journal homepage: www.elsevier.com/locate/jece

Engineered $ZnS:SnS_2/Bi_2S_3$ hierarchically porous heterostructure with accelerated charge transfer for trace level electrochemical detection of azathioprine

Kumar Gokulkumar [a], Neeraja Bose [a], Shih-Hsuan Chen [a], Sakthivel Kogularasu [e,f], Barani Kumar Duvaragan [g], Kun-Mu Lee [a,b,c,d,*]

[a] Center for Sustainability and Energy Technologies, Chang Gung University, Taoyuan 33302, Taiwan
[b] Department of Chemical and Materials Engineering, Chang Gung University, Taoyuan 33302, Taiwan
[c] Division of Neonatology, Department of Pediatrics, Chang Gung Memorial Hospital, Linkou, Taoyuan 33305, Taiwan
[d] College of Environment and Resources, Ming Chi University of Technology, New Taipei City 24301, Taiwan
[e] Super Micro Mass Research and Technology Center, Cheng Shiu University, Kaohsiung 833301, Taiwan
[f] Center for Environmental Toxin and Emerging-Contaminant Research, Cheng Shiu University, Kaohsiung 833301, Taiwan
[g] Centre for Applied Nanomaterials, Chennai Institute of Technology, Chennai, Tamil Nadu 00069, India

ARTICLE INFO

Keywords:
Environmental detection
Hierarchically porous heterostructure
Sulfide nanocomposite
Differential pulse voltammetry
Electrochemical sensing

ABSTRACT

The persistent challenge in electrochemical sensing lies in achieving high selectivity and reproducibility for reliable contaminant monitoring. Previously explored mixed sulfides such as $ZnS:SnS_2$ have attracted considerable attention due to their favorable electrolyte diffusion pathways and abundant electroactive sites that enhance analyte interaction. In this work, Bi_2S_3 was integrated onto the $ZnS:SnS_2$ framework through a combined hydrothermal–ultrasonication approach to construct a hierarchically porous $ZnS:SnS_2/Bi_2S_3$ heterostructure for the sensitive detection of azathioprine (AZA), an emerging pharmaceutical contaminant. The obtained heterostructure exhibited a surface area of 16.42 $m^2\ g^{-1}$ and delivered excellent electrochemical sensing performance with an ultralow detection limit of 0.0012 μM, a sensitivity of 0.52 $\mu A\ \mu M^{-1}\ cm^{-2}$, and two broad linear ranges of 0.0025–610.25 μM and 711.50–1420.75 μM. The enhanced interfacial charge-transfer behavior of Type-II heterointerfacial charge transfer, improved electron migration, and strong AZA adsorption affinity within the coupled sulfide domains. The $ZnS:SnS_2/Bi_2S_3$/GCE retained 96% of its initial response after 30 days, exhibiting excellent repeatability (RSD: 0.24%) and reproducibility (RSD: 0.31%), reflecting the robust interfacial stability of the heterostructure during repeated electrochemical cycling. Furthermore, recovery values ranging from 97.6% to 101.2% obtained from environmental water samples confirm the practical applicability of the developed sensor for pharmaceutical contaminant monitoring.

1. Introduction

Azathioprine (AZA) is a purine-analogue antimetabolite widely prescribed for the management of immune-mediated disorders, including Crohn's disease, rheumatoid arthritis, ulcerative colitis, pemphigus, and post-transplant immunosuppression [1–3]. It is also administered in high doses for certain dermatological conditions, as highlighted by the National Eczema Society in the UK. Despite its therapeutic relevance [4], AZA presents substantial clinical risks due to its narrow therapeutic index. Prolonged use has been linked to lymphoma, leukemia, and aggressive skin cancers, while even moderate dosing can induce severe myelotoxicity, suppressing erythrocytes, leukocytes, and thrombocytes Such hematological suppression may result in life-threatening infections, anemia, and impaired blood clotting [5–8].Therefore, precise and routine monitoring of AZA concentrations is essential to prevent systemic overdose, guide dosage adjustments, and ensure patient safety. These urgent toxicological concerns underscore the need for frequent, accurate, and cost-effective AZA detection strategies.

Conventional analytical platforms such as SERS [9], NMR spectroscopy [10], chemiluminescence [11], and HPLC [12] offer high analytical accuracy; however, they are limited by long analysis times,

* Corresponding author at: Department of Chemical and Materials Engineering, Chang Gung University, Taoyuan 33302, Taiwan.
E-mail address: kmlee@mail.cgu.edu.tw (K.-M. Lee).

https://doi.org/10.1016/j.jece.2026.123587
Received 8 March 2026; Received in revised form 21 May 2026; Accepted 11 June 2026
Available online 12 June 2026

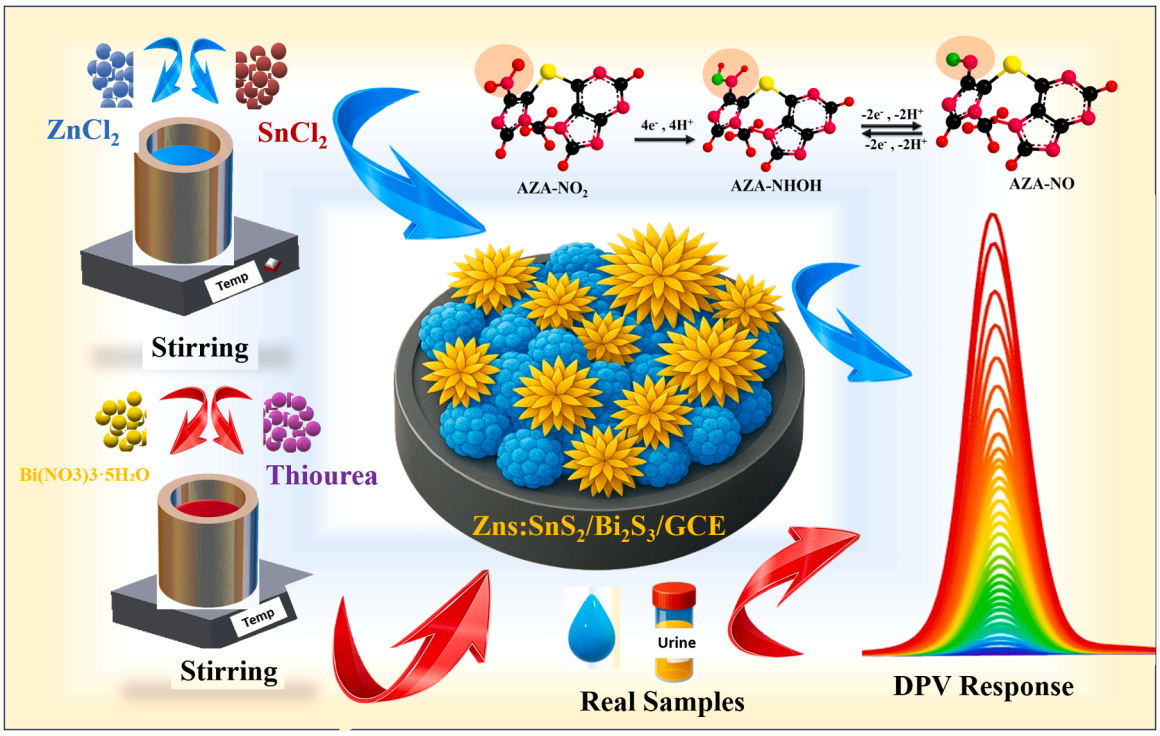

Scheme 1. Schematic representation of the synthesis of the ZnS:SnS_2/Bi_2S_3 composite, its coating on the GCE, and the electrochemical detection of AZA.

expensive instrumentation, complex sample preparation, and the need for highly trained personnel. These limitations have driven increasing interest in portable electrochemical sensors, which provide rapid response, low detection limits, and compatibility with compact, miniaturized systems [13,14]. The performance of such sensors is strongly influenced by the physicochemical properties of the modified glassy carbon electrode (GCE) [15,16]. In this context, cyclic voltammetry (CV) provides valuable insight into redox transformation, while differential pulse voltammetry (DPV) enhances faradaic signals through pulsed potential inputs, enabling high sensitivity and nM-level quantification [17–19]. Effective AZA detection therefore requires electrode surfaces with high electron mobility, strong adsorption affinity, and stable redox kinetics, particularly because AZA undergoes a complex, multi-step proton-coupled electron transfer process.

In recent years, a wide range of functional materials particularly metal chalcogenides has been explored for electrochemical application due to their tunable electronic structures, rich surface chemistry, and ability to multiple redox-active sites [20–22]. Among mixed sulfide systems, ZnS:SnS_2 has attracted attention due to its favorable electrochemical characteristics, including enhanced electrolyte diffusion and abundant electroactive sites arising from its porous structural framework [23–25]. The layered SnS_2 component contributes strong surface activity, while ZnS improves structural stability and provides additional catalytic centers, collectively promoting efficient analyte interaction and electron transport [26,27]. In contrast, Bi_2S_3 possesses relatively higher electrical conductivity and strong affinity toward nitrogen- and sulfur-containing molecules [28]. Its flower-like morphology exposes numerous active edge and defect sites that facilitate charge migration and molecular adsorption. [29]

By integrating ZnS:SnS_2 with Bi_2S_3 into a hierarchically porous heterostructure, the composite acquires electronic and structural advantages beyond those of the individual sulfides. The strongly coupled interface is expected to generate a band-aligned heterojunction [30–32], which facilitates directional electron migration across the sulfide interfaces and accelerates interfacial charge-transfer kinetics during the electrochemical reduction of AZA. This enhanced electron transport promotes rapid proton-coupled electron transfer between AZA molecules and the electrode surface, resulting in amplified reduction current and improved sensing sensitivity. In addition, the hierarchically porous framework improves electrolyte penetration, exposes abundant edge and defect sites, and supports rapid diffusion and adsorption of AZA molecules. Together, these features create a highly conductive and accessible sensing interface that enhances current response, sensitivity, and operational stability [33,34].

In this work, we developed a ZnS:SnS_2/Bi_2S_3 hierarchically porous heterostructure using hydrothermal and ultra-sonochemical routes, yielding a uniformly integrated composite with enhanced charge mobility, abundant active sites, and strong AZA affinity. This is the first report demonstrating AZA detection using this engineered sulfide heterojunction. The ZnS:SnS_2/Bi_2S_3/GCE delivered two broad linear ranges ($R^2 = 0.977$ for 0.0025–610.25 μM; $R^2 = 0.990$ for 711.50–1420.75 μM), an ultralow LOD of 0.0012 μM, and a high sensitivity of 0.52 μA μM^{-1} cm^{-2}. These superior analytical metrics arise from the electron transport across the interface and the hierarchically porous network that accelerates diffusion and strengthens AZA adsorption. The sensor also showed excellent performance in tap water, river water, and human urine with high recoveries, confirming its practicality for real-sample Enviromental and pharmaceutical monitoring in Scheme 1.

2. Chemicals and methods

The detailed descriptions of all chemicals, synthesis procedures, and instrumental techniques are provided in the supplementary material (**Sections S1 and S2**).

2.1. *Synthesis of ZnS:SnS_2 heterostructure*

In a standard preparation, aqueous solutions of $ZnCl_2$ (0.1 M) and $SnCl_2$ (0.1 M) were first prepared individually by dissolving the salts in 40 mL of deionized water and stirring for 15 min. The $SnCl_2$ solution was then introduced slowly into the zinc precursor under gentle agitation to promote uniform mixing of the metal ions. In a separate step, the

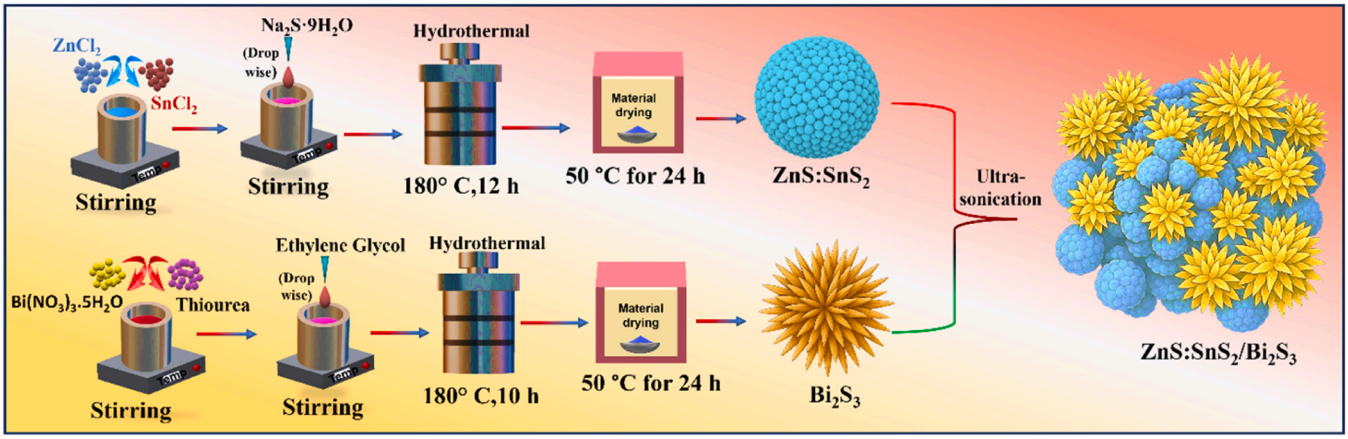

Scheme 2. Schematic representation of the hydrothermal formation of $ZnS:SnS_2$ and Bi_2S_3, and the subsequent ultrasonication-driven interfacial assembly that yields the $ZnS:SnS_2/Bi_2S_3$ composite.

required amount of $Na_2S{\cdot}9\ H_2O$ was dissolved in 10 mL of DI water and subsequently added dropwise into the mixed Zn–Sn solution, initiating the formation of sulfide nuclei. The appearance of a light, uniform precipitate confirmed the onset of $ZnS:SnS_2$ nucleation. The resulting mixture was transferred to a Teflon-lined stainless steel autoclave and subjected to hydrothermal treatment at 180 °C for 12 h. After cooling to room temperature, the solid product was isolated by centrifugation, washed several times with DI water and ethanol to eliminate residual ions, and dried at 50 °C for 24 h [35]. The final material was labeled as $ZnS:SnS_2$

2.2. Synthesis of Bi_2S_3 nanostructures

For the preparation of Bi_2S_3, a 0.1 M solution of $Bi(NO_3)_3{\cdot}5\ H_2O$ was first prepared in 40 mL of deionized water, after which the appropriate amount of thiourea was introduced and the mixture was stirred for 30 min to ensure complete dissolution. To improve precursor compatibility and regulate the nucleation process, 10 mL of ethylene glycol was added gradually, and the solution was stirred for an additional 15 min. The resulting homogeneous mixture was transferred into a Teflon-lined stainless-steel autoclave and subjected to hydrothermal treatment at 180 °C for 10 h. After the reactor cooled naturally, the dark precipitate was collected, repeatedly rinsed with DI water and ethanol to remove residual by-products, and dried at 50 °C. The obtained material was designated as Bi_2S_3.[29]

2.3. Preparation of $ZnS:SnS_2/Bi_2S_3$ composite

To assemble the hybrid heterostructure, equal masses(1:1 ratio) of $ZnS:SnS_2$ and Bi_2S_3 were dispersed in 40 mL of deionized water and sonicated for 45 min to promote intimate contact between the two components. During this process, the Bi_2S_3 nanosheets gradually adhered to the surfaces of the $ZnS:SnS_2$ nanospheres, aided by sulfur-mediated interfacial bonding and electrostatic attraction. The suspension was subsequently stirred for an additional 3 h to strengthen the junctions and ensure uniform heterostructure development. The resulting composite was isolated by centrifugation, rinsed thoroughly, and dried at 50 °C to obtain the final $ZnS:SnS_2/Bi_2S_3$ material. The overall synthesis and interfacial assembly steps are summarized schematically in Scheme 2. A 1:1 mass ratio between $ZnS:SnS_2$ and Bi_2S_3 was adopted to promote uniform heterointerfacial integration and maintain balanced structural and electrochemical contributions from both sulfide domains. This composition was selected based on previously reported sulfide heterostructure strategies, where comparable phase distribution facilitates efficient interfacial charge-transfer pathways and stable composite formation [36–38].

2.4. Ink preparation and electrode fabrication

To formulate the catalyst ink, 2 mg of the $ZnS:SnS_2/Bi_2S_3$ composite was dispersed in 3 mL of deionized water and ultrasonicated for 30 min to produce a homogeneous and stable suspension. The GCE (3 mm diameter) was polished with 0.05 μm alumina slurry, thoroughly rinsed with deionized water, and gently dried under a nitrogen stream to ensure a clean, electroactive surface. A 6 μL aliquot of the prepared ink was then drop-cast onto the polished GCE and dried at 60 °C, resulting in a uniform and well-adhered catalytic film. The modified electrode, designated as $ZnS:SnS_2/Bi_2S_3$/GCE, was subsequently employed for all electrochemical measurements. No additional polymeric binder was employed during electrode fabrication. The stable immobilization of the $ZnS:SnS_2/Bi_2S_3$/GCE composite on the GCE surface is attributed to the strong interfacial interaction and interconnected porous morphology of the heterostructure, which promotes effective physical adhesion to the electrode surface. Furthermore, the excellent repeatability, reproducibility, and long-term stability results confirm that the binder-free sensing layer remained structurally stable during repeated electrochemical measurements [39].

3. Results and discussions

3.1. XRD analysis

The crystalline structure and phase composition of the synthesized materials were verified using X-ray diffraction (XRD), as shown in Fig. 1**A**. The Bi_2S_3 exhibited characteristic diffraction peaks at 2θ values of 22.5°, 24.8°, 27.4°, 31.8°, 34.3°, and 44.6°, which correspond to the (130), (211), (221), (431), (002), and (122) crystal planes of orthorhombic Bi_2S_3 (JCPDS No. 01–017–0320). The sharpness of these reflections indicates the highly crystalline nature of the synthesized Bi_2S_3 phase, and the absence of extraneous peaks confirms its phase purity. For the $ZnS:SnS_2$ binary system, distinct peaks located at 28.5°, 47.6°, and 56.4° are indexed to the (111), (220), and (311) planes of cubic ZnS (JCPDS No. 01–007–2100) [40]. Similarly, additional reflections appearing near 16.5°, 50.1°, and 52.5° correspond to the (101), (110), and (119) planes of rhombohedral SnS_2 (JCPDS No. 00–040–1466) [41], confirming the successful formation of a coupled $ZnS:SnS_2$ heterostructure. The coexistence of these reflections with no impurity phases demonstrates effective incorporation of ZnS and SnS_2 within the composite lattice. In the case of the $ZnS:SnS_2/Bi_2S_3$ composite, all major diffraction peaks of Bi_2S_3, ZnS, and SnS_2 are retained without any secondary phase formation, implying that the integration of Bi_2S_3 did not disturb the crystal framework of the $ZnS:SnS_2$ matrix. The composite shows slightly broadened diffraction peaks compared to the individual

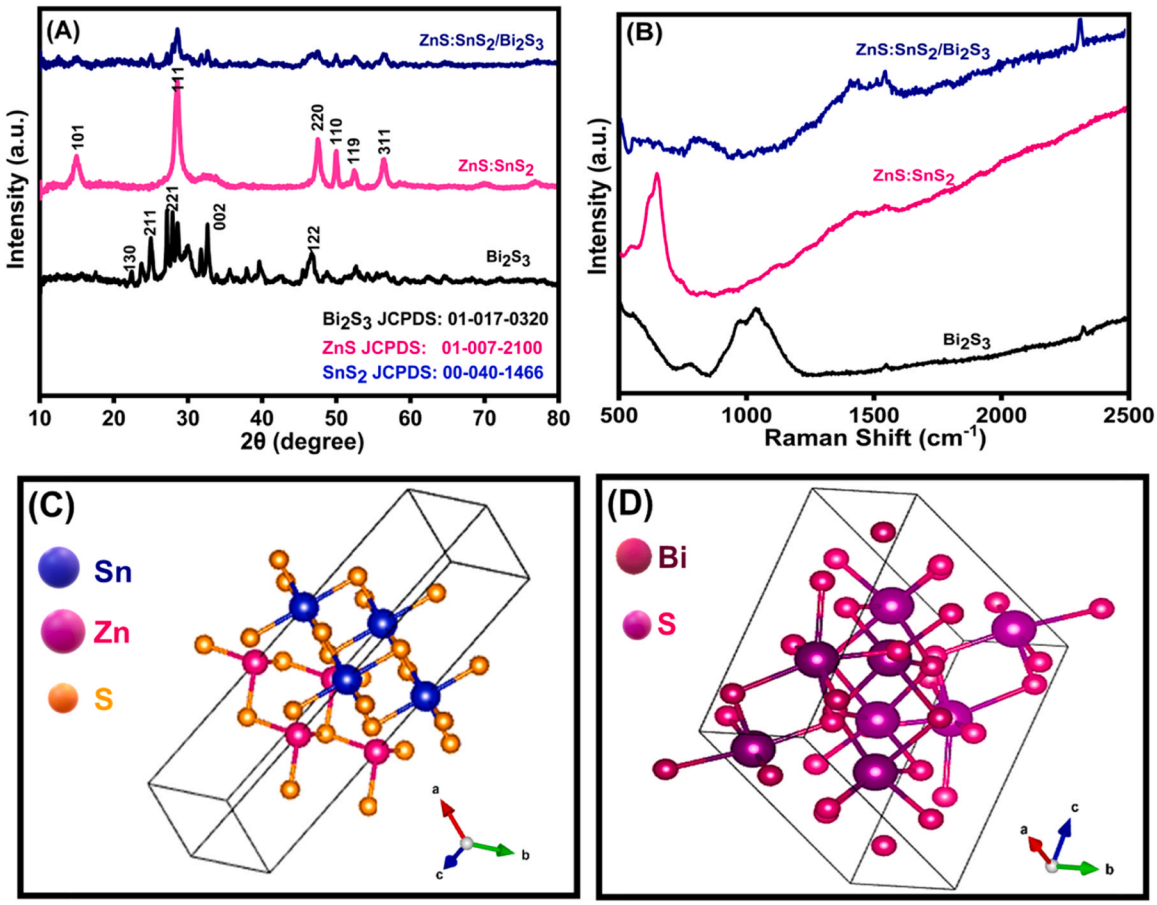

Fig. 1. (A) XRD patterns of Bi_2S_3, ZnS:SnS_2, and the ZnS:SnS_2/Bi_2S_3 composite, confirming the coexistence of both phases without impurity formation. (B) Raman spectra of Bi_2S_3, ZnS:SnS_2, and ZnS:SnS_2/Bi_2S_3, showing their characteristic vibrational modes and structural integrity after composite formation. (C) Crystal structure model of ZnS:SnS_2, illustrating the coordination environment of Zn, Sn, and S atoms. (D) Crystal structure of Bi_2S_3, showing Bi–S atomic arrangement within the layered lattice.

components, suggesting a decrease in crystallite size and possible lattice strain induced by interfacial coupling between the sulfide domains. The presence of well-defined peaks across all phases verifies the formation of a ternary chalcogenide heterostructure ZnS:SnS_2/Bi_2S_3 with high structural stability and intimate interfacial contact an advantageous feature for efficient charge transport in electrochemical applications.

3.2. Raman analysis

Raman spectroscopy was employed to validate the chemical structure and interfacial interaction of the prepared materials, and the corresponding spectra are illustrated in Fig. 1**B.** The pristine Bi_2S_3 displayed characteristic vibrational bands at 250, 420, 610, and 965 cm^{-1}, which are assigned to the intrinsic Bi–S lattice vibrations of orthorhombic Bi_2S_3 confirming its good crystallinity and phase purity [42]. For the ZnS:SnS_2 system, two major Raman modes were observed at around 311.8 cm^{-1} and 469 cm^{-1}, corresponding respectively to the $A_{1\,g}$ vibration of SnS_2 and the Zn–S stretching mode of ZnS. The coexistence of both sets of peaks confirms the successful coupling of ZnS and SnS_2 within the heterostructure [43,44]. ZnS:SnS_2/Bi_2S_3 composite, all the characteristic Raman peaks of the individual phases are preserved but appear broadened and slightly shifted, reflecting lattice strain and strong interfacial coupling between the Bi_2S_3 and ZnS:SnS_2 frameworks. The merging and red-shift of the Bi–S and Zn–S:Sn–S_2 modes indicate enhanced phonon coupling and electronic interaction at the interface. Such structural synergy is beneficial for rapid charge transport and reduced recombination, consistent with the improved electrochemical behaviour observed for the composite.

3.3. Crystal structure and Interface

Fig. 1**C and D** depict the crystal structures of the individual components. The ZnS:SnS_2 lattice consists of Zn, Sn, and S atoms arranged in a layered configuration, where Zn and Sn are coordinated with sulfur atoms to form a stable semiconducting framework. The Bi_2S_3 structure, on the other hand, adopts an orthorhombic arrangement with Bi–S chains extending along one direction, providing high conductivity and abundant surface-active sites. When these two chalcogenides are integrated, the close contact between their lattice planes enables strong S–S interfacial bonding and efficient orbital overlap. This coupling forms a stable heterojunction interface, which facilitates directional charge transfer and suppresses electron–hole recombination. As a result, the ZnS:SnS_2/Bi_2S_3 heterostructure combines high charge mobility with enhanced conductivity, offering significant advantages for electrochemical and catalytic applications.

3.4. XPS analysis

The surface chemical states of the ZnS:SnS_2/Bi_2S_3 composite were examined by XPS, and the high-resolution spectra are shown in Fig. 2**A–D**. The Sn 3d spectrum Fig. 2**A** displays two distinct peaks at 486.5 eV and 495.0 eV, corresponding to Sn $3d_{5/2}$ and Sn $3d_{3/2}$, which confirm the Sn^{4+} state of SnS_2. [45]In Fig. 2**B**, the Zn 2p spectrum exhibits two peaks at 1021.8 eV Zn $2p_{3/2}$ and 1045.1 eV Zn $2p_{1/2}$, characteristic of Zn^{2+} in ZnS. The Bi 4 f region [46] Fig. 2**C** shows two strong peaks at 158.9 eV Bi 4 $f_{7/2}$ and 164.2 eV Bi 4 $f_{5/2}$, confirming the oxidation state of Bi^{3+} in Bi_2S_3. In the S 2p spectrum [47] Fig. 2**D,** the

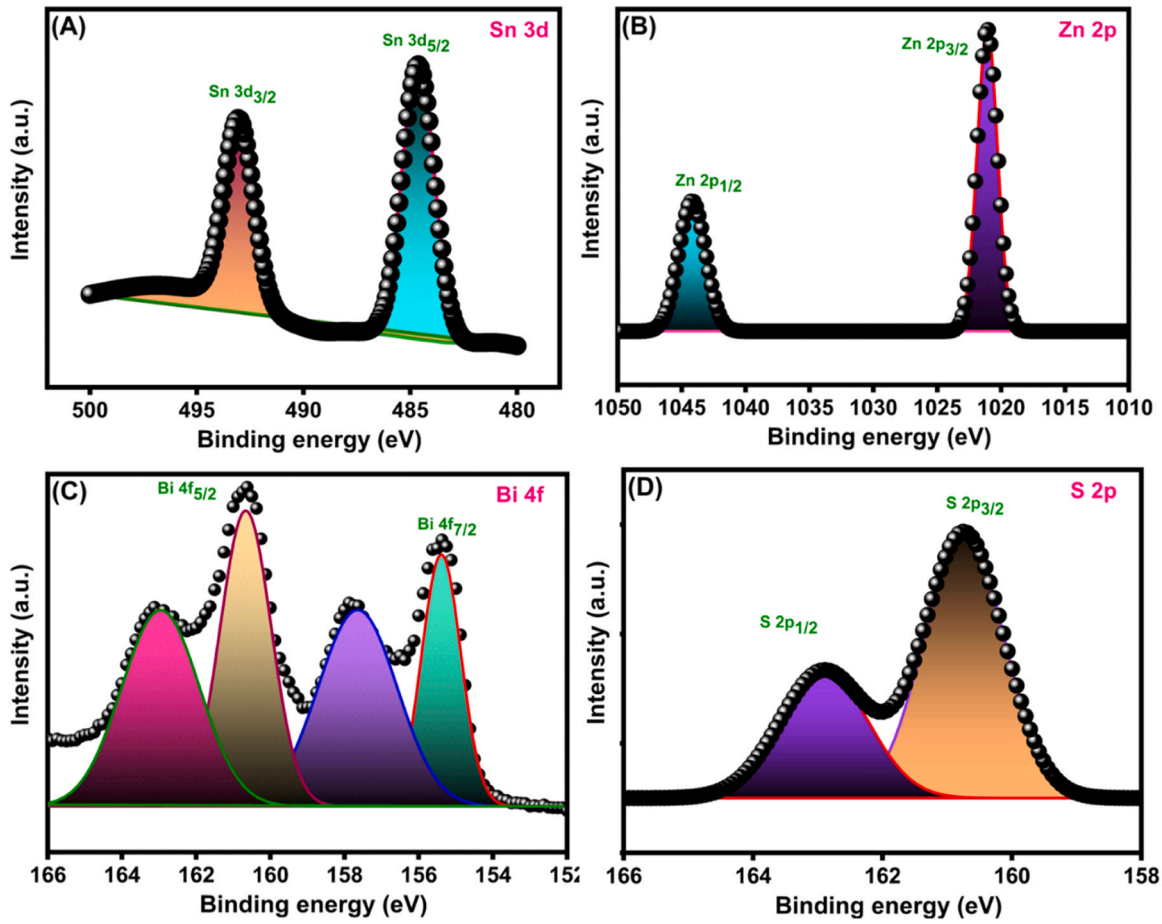

Fig. 2. High-resolution XPS spectra of the ZnS:SnS_2/Bi_2S_3 composite. (A) The Sn 3d spectrum displays the Sn $3d_{5/2}$ and Sn $3d_{3/2}$ features, confirming the presence of Sn^{4+} associated with the SnS_2 phase. (B) The Zn 2p region exhibits well-defined Zn $2p_{3/2}$ and Zn $2p_{1/2}$ peaks, characteristic of Zn^{2+} in ZnS. (C) The Bi 4 f spectrum shows the Bi 4 $f_{7/2}$ and Bi 4 $f_{5/2}$ components, indicating Bi^{3+} states typical of Bi_2S_3. (D) The S 2p spectrum presents the S $2p_{3/2}$ and S $2p_{1/2}$ doublets, reflecting metal–sulfur coordination within the composite framework.

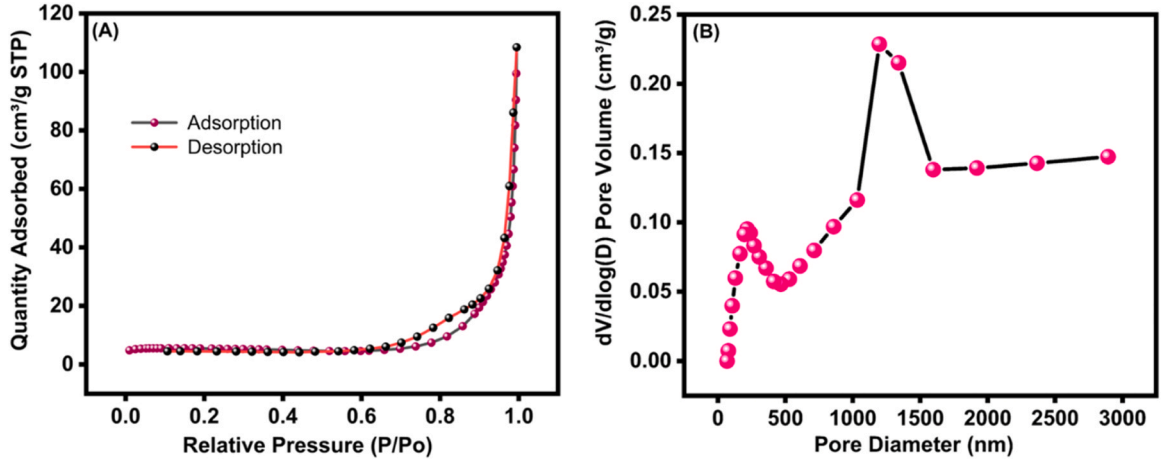

Fig. 3. Nitrogen adsorption–desorption analysis of the ZnS:SnS_2/Bi_2S_3 composite. (A) N_2 adsorption–desorption isotherms recorded at 77 K, exhibiting a type-IV isotherm with a distinct hysteresis loop, indicative of a hierarchically porous structure. (B) Corresponding pore size distribution derived from the BJH method, revealing a broad hierarchically porous distribution.

doublet peaks located at 161.9 eV S $2p_{3/2}$ and 163.2 eV S $2p_{1/2}$ are attributed to S^{2-} species bonded to Zn, Sn, and Bi atoms. Notably, a slight positive shift in the binding energies of Sn 3d, Zn 2p, and S 2p is observed compared with the pure components, indicating electronic interaction and charge redistribution among ZnS:SnS_2 and Bi_2S_3 domains. These shifts arise from the formation of a heterointerface, where S atoms serve as bridging sites linking Bi–S, Zn–S, and Sn–S bonds. This confirms the establishment of strong interfacial coupling and validates the chemical integrity of the ZnS:SnS_2/Bi_2S_3 heterostructure.

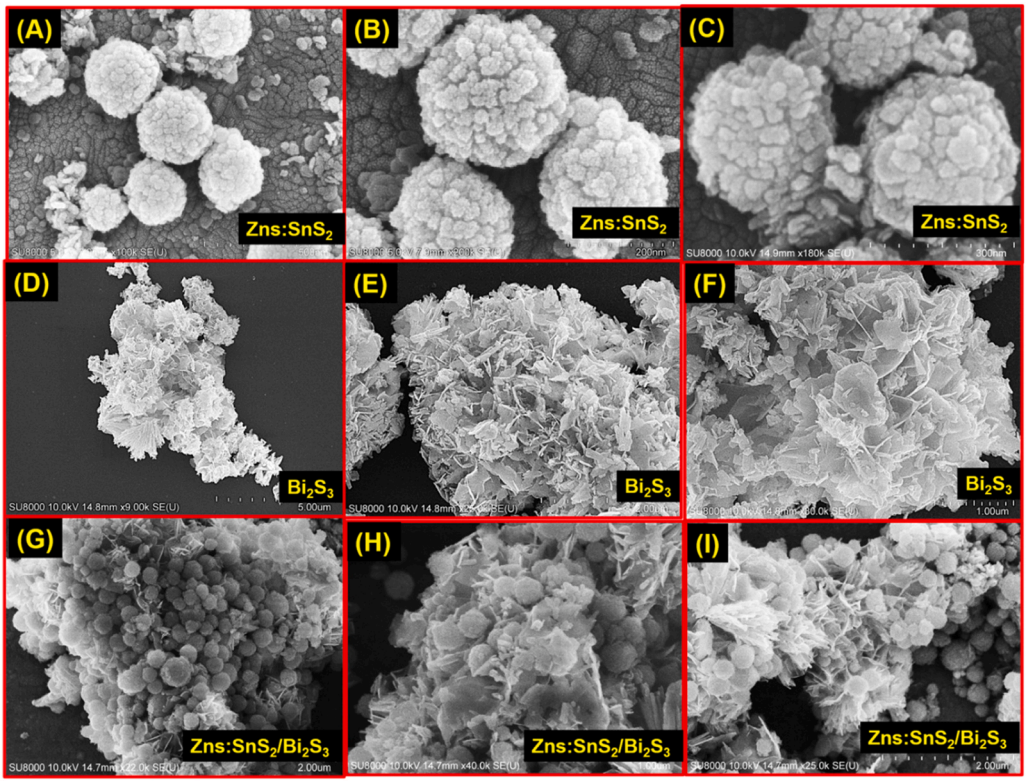

Fig. 4. FESEM images of (A–C) ZnS:SnS_2 showing clustered spherical nanostructures, (D–F) Bi_2S_3 with flower-like nanosheet assemblies, and (G–I) the ZnS:SnS_2/Bi_2S_3 composite where Bi_2S_3 is uniformly anchored onto the ZnS:SnS_2 spheres.

3.5. BET analysis

Nitrogen adsorption–desorption measurements were conducted to elucidate the textural properties and pore evolution within the ZnS:SnS_2/Bi_2S_3 heterostructure. The resulting isotherm Fig. 3**A.** displays a characteristic type-IV profile accompanied by a pronounced H3 hysteresis loop, indicative of a hierarchically porous framework. This behavior suggests the presence of pores and interlayer voids, reflecting the layered morphology and open channels formed during composite assembly. The H3 hysteresis, typically associated with aggregates of plate-like or flower-like particles, directly reflects the hierarchical morphology observed in the FESEM and TEM micrographs where Bi_2S_3 nanosheets and ZnS:SnS_2 nanospheres interconnect to create open, non-rigid mesopores. The initial portion of the isotherm $<P/Po = 0.3$ shows a very small uptake, indicating negligible microporosity, while the rapid increase in adsorbed volume at higher relative pressures $P/Po \rightarrow 1$ corresponds to capillary condensation in meso–macropore domains, typical of hierarchical sulfide-based assemblies. This behavior aligns well with the structural complexity of the composite and confirms the presence of abundant interparticle hierarchically porous created by loose packing of flower-like Bi_2S_3 structures and spherical ZnS:SnS_2 domains. The BET surface area of the composite was calculated to be 16.42 m^2/g, a moderate value considering the dense atomic structure of metal sulfides.

The BJH pore-size distribution profile Fig. 3**B** further reveals a broad multimodal hierarchically porous, with pore diameters ranging predominantly from 100 nm to over 1500 nm, and a prominent peak \around ~1200–1300 nm. Such large meso–macropores are characteristic of materials with hierarchical open frameworks, resulting from the interweaving of two morphologically distinct sulfide phases. These wide channels serve as efficient mass-transport highways, enabling rapid electrolyte penetration and accelerating redox kinetics at the electrode–electrolyte interface. Moreover, the interconnected porous framework increases the accessible contact area between AZA molecules and the electroactive heterostructure surface, thereby facilitating efficient adsorption and promoting rapid proton-coupled electron-transfer processes during AZA reduction. The relatively high pore volume observed in the 0.1–0.22 cm^3/g region signifies that the composite possesses expansive void networks, which play a crucial role in preventing analyte trapping and enhancing diffusion-controlled electrochemical processes and fast analyte delivery to the active surface directly dictates sensitivity and response time.

3.6. AFM analysis

Atomic force microscopy (AFM) was employed to quantitatively evaluate the surface topography and roughness characteristics of the ZnS:SnS_2/Bi_2S_3 composite deposited on a glass substrate, which was used as a representative and smooth support for surface analysis. The AFM results reveal a pronounced increase in surface roughness after composite deposition, confirming successful immobilization of the heterostructured material. Based on surface analysis, the coated glass surface exhibits an average arithmetic roughness (Sa) of approximately 0.75 μm and a root-mean-square roughness (Sq) of ~1.04 μm, indicating the formation of a textured and heterogeneous surface. Localized regions with higher roughness values are attributed to the presence of composite aggregates distributed across the substrate. Such surface features are advantageous for electrochemical sensing, as they promote enhanced analyte adsorption and provide a larger number of accessible electroactive sites. The corresponding 3D AFM topography and optical surface image are provided in the Supplementary Information Fig. S2**.**

3.7. FESEM analysis

The surface morphology and structural characteristics of the prepared materials were examined by FE-SEM, as shown in Fig. 4**A–I**. The ZnS:SnS_2 micrographs Fig. 4**A–C** reveal well-defined spherical aggregates composed of compactly arranged nanograins. The uniform particle

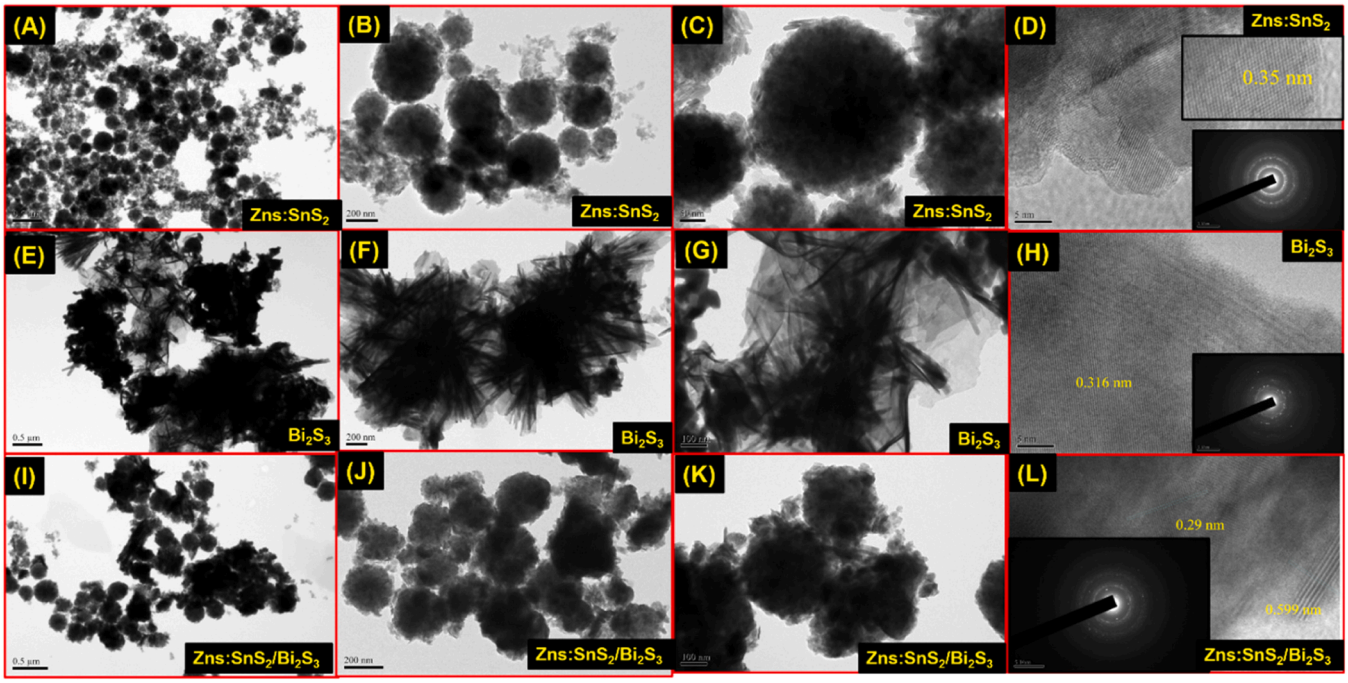

Fig. 5. TEM images of (A–C) ZnS:SnS_2 showing spherical nanoparticle clusters, (E–G) Bi_2S_3 displaying flower-like structures, and (I–K) the ZnS:SnS_2/Bi_2S_3 composite where Bi_2S_3 is uniformly anchored on ZnS:SnS_2 surfaces. HRTEM images (D, H, L) confirm clear lattice fringes and SAED ring patterns, verifying the crystalline nature and successful composite formation.

distribution indicates homogeneous nucleation and growth of ZnS and SnS_2 during the hydrothermal synthesis. Such morphology provides a large surface area and interconnected active sites favourable for electron transport and electrolyte access [35]. The Bi_2S_3 samples Fig. 4**D–F** exhibit irregular sheet-like clusters, which reflect the anisotropic growth nature of orthorhombic Bi_2S_3. These thin sheets are loosely stacked, generating open structures that can act as effective conductive channels and adsorption surfaces [29]. After hybridization, the ZnS:SnS_2/Bi_2S_3 composite Fig. 4**G–I** displays a distinct microstructure in which ZnS:SnS_2 spherical particles are uniformly anchored on the Bi_2S_3 nanosheets. The close interfacial contact between these two morphologies confirms strong physical and chemical interaction, forming a continuous conductive framework.

3.7.1. *Elemental mapping*

Energy-dispersive X-ray spectroscopy coupled with elemental mapping was employed to confirm both the elemental composition and spatial integration of the ZnS:SnS_2/Bi_2S_3 heterostructure are provided in the supplementary material Fig. S1 The EDS spectrum verifies the presence of Zn, Sn, Bi, and S as the sole constituent elements, with no extraneous signals detected, indicating high compositional purity. The corresponding elemental maps reveal a highly uniform distribution of all elements across the selected region. Sulfur exhibits a continuous and intense signal throughout the matrix, reflecting its structural role in linking the ZnS, SnS_2, and Bi_2S_3 phases. Meanwhile, the Zn, Sn, and Bi maps show well-overlapped and evenly dispersed signals, demonstrating intimate interfacial contact between the individual sulfide components. Such spatial coherence confirms the successful formation of a chemically integrated heterostructure rather than a physical mixture, which is expected to facilitate efficient charge transport across the interfaces and contribute to the enhanced electrochemical performance of the composite.

3.8. *Transmission electron microscopy (TEM) analysis*

The detailed microstructural features of the prepared materials were examined by TEM, as shown in Fig. 5**A–L**. The ZnS:SnS_2 micrographs Fig. 5**(A–C)** display well-defined spherical nanostructures with diameters of approximately 150–250 nm. The individual particles are composed of compact nanograins, confirming a uniform and crystalline nature. The high-resolution TEM image Fig. 5**D** displays well-defined lattice fringes with measured spacings of 0.35 nm and 0.31 nm, which can be assigned to the (101) plane of SnS_2 and the (111) plane of cubic ZnS, respectively, in accordance with JCPDS files 01–007–2100 and 00–040–1466. The coexistence of both spacings within the same particle confirms the formation of a coupled ZnS:SnS2 heterostructure. The corresponding SAED pattern shows sharp concentric diffraction rings assignable to the (111), (220), and (311) planes of ZnS and the (100) and (110) planes of SnS_2, evidencing its polycrystalline nature.

The Bi_2S_3 TEM images Fig. 5**E–G** reveal a nanosheet-assembled network, showing long, thin, and flexible sheet-like features. The layered arrangement and interconnected morphology confirm the anisotropic growth of orthorhombic Bi_2S_3. The HRTEM image Fig. 5**H** shows clear lattice fringes with a measured spacing of 0.316 nm, corresponding to the (130) plane of orthorhombic Bi_2S_3, consistent with JCPDS 01–017–0320. The accompanying SAED pattern features well-defined diffraction rings indexed to the (120), (211), and (221) planes, indicating the high crystallinity and oriented growth characteristics of the Bi_2S_3 phase.

After hybridization, the ZnS:SnS_2/Bi_2S_3 composite Fig. 4**I–K** displays an intimate interfacial contact where ZnS:SnS_2 nanospheres are uniformly anchored onto Bi_2S_3 sheets. The HRTEM image Fig. 4**L** shows multiple lattice fringes with d-spacings of 0.35 nm SnS_2 (101), 0.31 nm ZnS (111), and 0.29 nm Bi_2S_3 (200), signifying strong interfacial coupling between all three sulfide phases. The composite's SAED pattern exhibits overlapping diffraction rings consistent with each component, verifying the coexistence of multiple crystalline domains within a unified heterostructure.

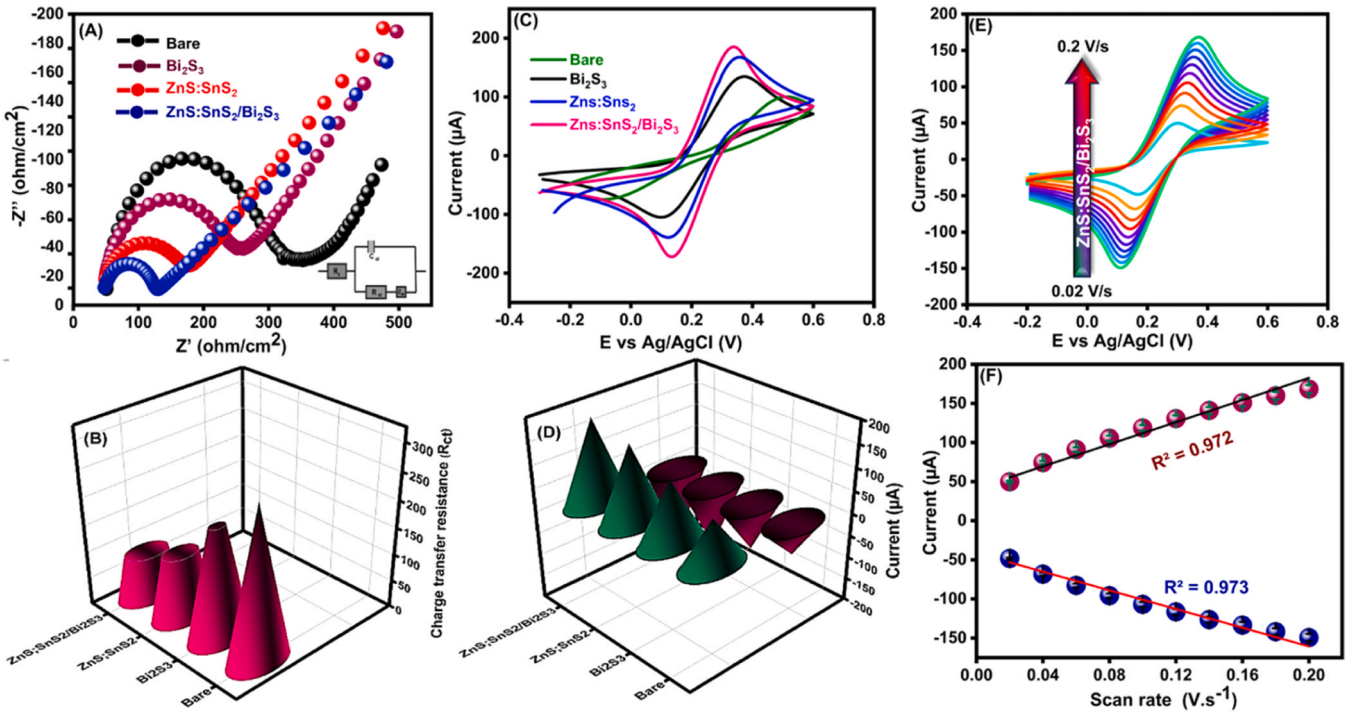

Fig. 6. (A) EIS Nyquist plots of bare GCE, Bi_2S_3/GCE, ZnS:SnS_2/GCE, and ZnS:SnS_2/Bi_2S_3 /GCE recorded in 5 mM $[Fe(CN)_6]^{3-/4-}$ 0.1 M KCl, showing a significant reduction in Rct after composite formation. (B) 3D visualization of the corresponding charge-transfer resistance values highlighting the enhanced conductivity of the ZnS:SnS_2/Bi_2S_3 composite. (C) CV responses of bare and modified electrodes confirming accelerated electron-transfer kinetics for the composite-modified interface. (D) 3D representation of peak current enhancement across the electrode series. (E) CV curves of ZnS:SnS_2/Bi_2S_3/GCE recorded at scan rates from 0.02 to 0.2 V·s^{-1}, indicating a diffusion-controlled process. (F) Linear relationship between peak current and scan rate, demonstrating excellent kinetic reversibility and stable redox behavior.

Table 1
Electrochemical Parameters Obtained from EIS and Calculated Ks.

Electrode	Rct (Ω)	Cdl (μF)	Zw (Ω)	ks (cm·s^{-1})
Bare GCE	350	4.8	132	1.7×10^{-7}
Bi_2S_3/GCE	250	8.6	115	2.9×10^{-7}
ZnS:SnS_2/GCE	160	13.2	95	4.0×10^{-7}
ZnS:SnS_2/Bi_2S_3/GCE	100	17.9	78	5.6×10^{-7}

3.9. Electrochemical characterization

3.9.1. Electrochemical impedance spectroscopy (EIS)

Electrochemical impedance spectroscopy was performed in 0.1 M KCl containing 5 mM $[Fe(CN)_6]^{3-/4-}$ to assess the charge-transfer characteristics of the bare and modified GCEs. The Nyquist plots Fig. 6**A** display a semicircle in the high-frequency region, representing the charge-transfer resistance (Rct), followed by a linear Warburg region at lower frequencies associated with diffusion. The unmodified GCE exhibits the largest semicircle, with an Rct of 350 Ω, reflecting slow electron-transfer kinetics. Introducing Bi_2S_3 onto the electrode surface reduces Rct to 250 Ω, indicating that the semiconducting Bi_2S_3 structure enhances interfacial conductivity. A more pronounced decrease to 160 Ω is observed for the ZnS:SnS_2-modified electrode, which can be attributed to its shows higher surface area, abundant electroactive sites, and more efficient electron-hopping channels within the hybrid ZnS:SnS_2 framework.

Remarkably, the ZnS:SnS_2/Bi_2S_3 composite electrode displays the smallest semicircle with an Rct value of only 100 Ω, demonstrating superior conductivity and rapid charge-transfer behavior. The significant decline in Rct compared to the individual components confirms the formation of an efficient heterojunction interface that facilitates faster electron transport. The intimate coupling between the n-type ZnS:SnS_2 and Bi_2S_3 phases enhances charge carrier separation and lowers interfacial energy barriers, thus accelerating redox kinetics. The corresponding 3D impedance plots Fig. 6**B** clearly illustrate the descending trend in Rct bare GCE > Bi_2S_3 > ZnS:SnS_2 > ZnS:SnS_2/Bi_2S_3, validating the improvement in interfacial electron transfer upon hybrid formation. The electrochemical parameters obtained from EIS fitting and ks calculations are summarized in Table 1, which clearly demonstrate the progressive reduction in Rct and increase in Cdl with successive surface modification. The impedance behavior can be interpreted using a simplified Randles-type equivalent circuit **(Inset** Fig. 6**A)** consisting of solution resistance (Rs), charge-transfer resistance (Rct), double-layer capacitance (Cdl), and Warburg diffusion impedance (Zw). The observed decrease in Rct after heterostructure formation reflects enhanced interfacial conductivity and more efficient electron-transfer pathways across the coupled sulfide domains.

3.9.2. Cyclic voltammetry (CV) analysis

CV was carried out in 0.1 M KCl containing 5 mM $[Fe(CN)_6]^{3-/4-}$ to further evaluate the redox behavior and charge transfer efficiency of the modified electrodes. As shown in Fig. 6**C**, the bare GCE exhibits broad, weak redox peaks with a large peak to peak separation ΔEp ≈ 155 mV, indicating sluggish and quasi-irreversible electron transfer. Upon modification with Bi_2S_3, the current response increases moderately and ΔEp decreases to ~128 mV, confirming enhanced surface conductivity due to the semiconducting Bi_2S_3 layer. The ZnS:SnS_2 modified electrode shows a sharper redox pair with higher current density and a further reduced ΔEp ~102 mV, which can be attributed to the coupled Zn^{2+}/Sn^{4+} redox centers and high electron mobility within the nanostructured framework. Notably, the ZnS:SnS_2/Bi_2S_3 composite electrode delivers the highest anodic and cathodic current responses with the smallest ΔEp ~82 mV, signifying rapid and reversible charge-transfer kinetics. This improvement arises from the interface between ZnS:SnS_2 and Bi_2S_3, which promotes efficient carrier separation and establishes a continuous

Table 2
The calculated electroactive areas.

Electrode	Anodic Peak Current (μA)	ΔEp (mV)	Electroactive Area (cm^2)
Bare GCE	18.7	155	0.031
Bi_2S_3/GCE	27.3	128	0.048
ZnS:SnS_2/GCE	38.2	102	0.067
ZnS:SnS_2/Bi_2S_3/GCE	59.6	82	0.091

conductive network for fast ion and electron diffusion. The heterojunction formation reduces the interfacial potential barrier, facilitating efficient charge migration and electron delocalization across the hybrid surface.

To investigate the redox behavior, cyclic voltammograms were collected at scan rates ranging from 0.02 to 0.2 $V{\cdot}s^{-1}$ Fig. 6**E**. The peak currents increased proportionally with the square root of the scan rate, indicating that the electron-transfer process is predominantly diffusion controlled while maintaining quasi-reversible characteristics. This trend is further supported by the strong linear correlation between both anodic and cathodic peak currents and the square root of the scan rate (R^2 = 0.972 and 0.973), as shown in Fig. 6**F**, confirming stable and reproducible redox kinetics at the electrode interface. The enhanced current response and decreased ΔEp of the ZnS:SnS_2/Bi_2S_3/GCE demonstrate a substantial increase in electroactive surface area and faster charge-transfer kinetics, which are essential for its superior electrocatalytic sensing performance. Similarly, the electroactive surface area values calculated using the Randles–Ševčík equation **Eq-S1** [48] are listed in Table 2, confirming the significant enhancement in the available electroactive sites upon hybrid formation. The steady rise in surface area from 0.031 cm^2 bare GCE to 0.091 cm^2 ZnS:SnS_2/Bi_2S_3/GCE clearly validates the contribution of the enlarged surface roughness and heterointerface coupling to the overall charge-transfer kinetics.

3.10. Electrochemical behavior and optimization studies

3.10.1. Electrochemical reaction mechanism of AZA

During electrochemical sensing, the nitro-substituted form of

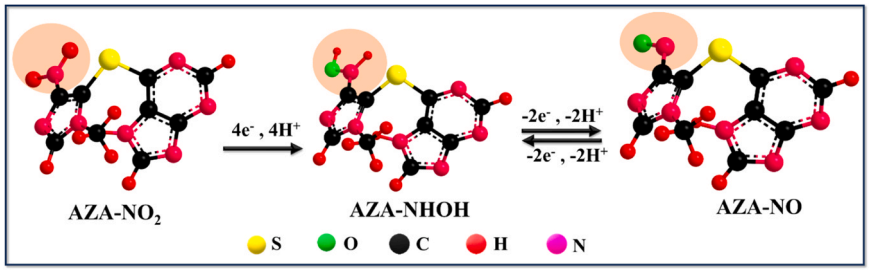

Scheme 3. Proposed electrochemical reduction mechanism of AZA showing the stepwise conversion of the –NO_2 group to –NHOH and subsequently to –NO through coupled electron proton transfer reactions.

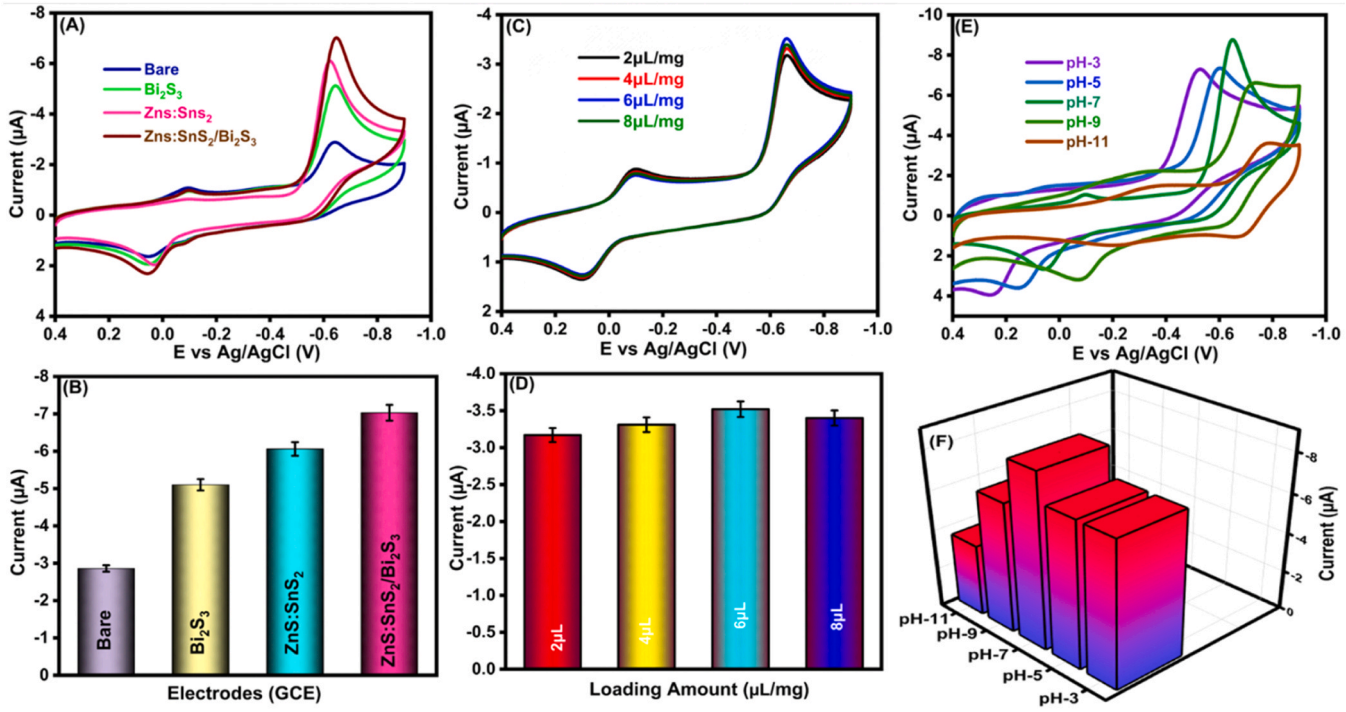

Fig. 7. (A) CV responses of bare GCE, Bi_2S_3/GCE, ZnS:SnS_2/GCE, and ZnS:SnS_2/Bi_2S_3 /GCE in PBS (pH 7), showing a progressive increase in peak current with composite formation. (B) Corresponding bar plot confirming the highest electrochemical activity for ZnS:SnS_2/Bi_2S_3/GCE due to its electron-transfer interface. (C) Effect of catalyst loading (2–8 μL/mg) on current response, indicating optimal signal at 6 μL/mg. (D) Bar representation of loading-dependent current changes. (E) CV responses at different pH conditions (pH 3–11), showing maximum current at pH 7. (F) 3D visualization of pH-dependent current variation, confirming that neutral medium provides the most favourable proton-coupled electron transfer environment.

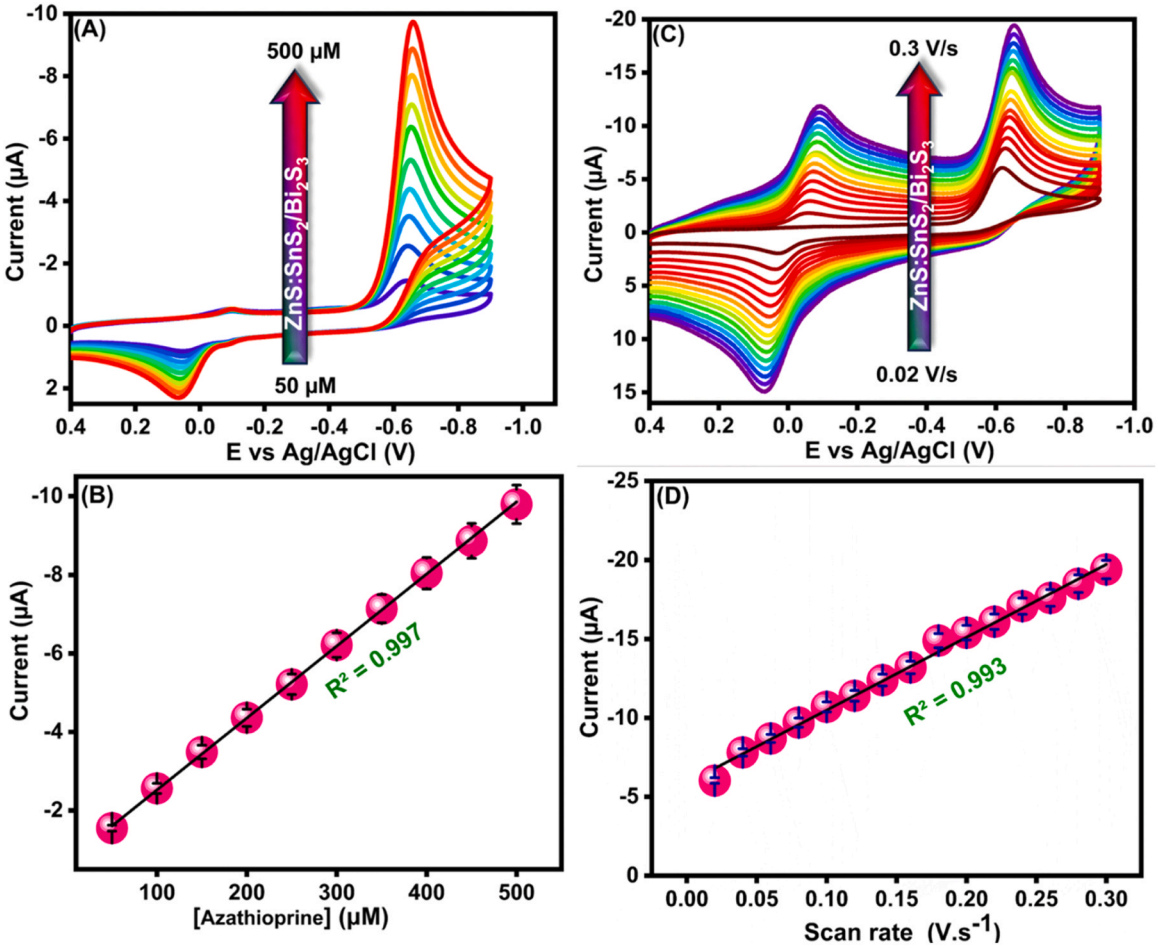

Fig. 8. (A) CV responses of the ZnS:SnS_2/Bi_2S_3 modified GCE toward increasing concentrations of azathioprine (50–500 µM). (B) Corresponding linear calibration plot showing an excellent correlation $R^2 = 0.997$ between current and analyte concentration. (C) CV curves of ZnS:SnS_2/Bi_2S_3/GCE at varying scan rates (0.02–0.3 V s^{-1}), indicating a surface-controlled process. (D) Linear relationship between peak current and scan rate $R^2 = 0.993$, confirming the electrode's efficient redox kinetics.

azathioprine (AZA–NO_2) undergoes a well-defined proton-coupled electron transfer (PCET) reduction pathway. Initially, the $-NO_2$ group is reduced through a four-electron and four-proton transfer process, forming the intermediate hydroxylamine species (AZA–NHOH). This conversion is facilitated by the high surface activity and electron-rich catalytic sites of the ZnS:SnS_2/Bi_2S_3 composite, which lowers the activation barrier for electron transfer. Subsequently, AZA–NHOH undergoes a reversible two-electron and two-proton redox transformation to form the nitroso derivative (AZA–NO) [49]. Scheme 3 illustrates this detailed reaction pathway, showing the multi-step electrochemical behavior of AZA on the proposed sensing platform. The enhanced electrochemical performance of the ZnS:SnS_2/Bi_2S_3 heterostructure arises from the combined electronic and structural contributions of the coupled sulfides. ZnS provides structural stability and electroactive sites, SnS_2 facilitates electron transport through its layered structure, while Bi_2S_3 improves conductivity and promotes AZA adsorption through its sulfur-rich surface. The coupled heterointerface is expected to facilitate directional electron migration, thereby accelerating proton-coupled electron-transfer kinetics during AZA reduction [32].

3.10.2. *Effect of electrode modification*

The electrochemical interaction of AZA with the prepared electrodes was systematically examined to understand the contribution of each component. As shown in Fig. 7**A**, the bare GCE displayed a weak and broad reduction peak due to poor conductivity and limited adsorption sites peak current (−2.86 µA). In contrast, the Bi_2S_3/GCE peak current (−5.07 µA) and ZnS:SnS_2/GCE peak current (−6.06 µA) showed enhanced redox responses, demonstrating that the semiconducting chalcogenides significantly accelerate electron transfer and provide electrochemically active surfaces. The ZnS:SnS_2/Bi_2S_3 heterostructure electrode exhibited the highest cathodic(−6.97 µA) current response, confirming the formation of an efficient charge-transfer interface. This enhancement arises from the band alignment between ZnS:SnS_2 and Bi_2S_3, which promotes directional electron migration from the conduction band of ZnS:SnS_2 to Bi_2S_3 minimizing recombination losses and boosting sensitivity. The bar chart Fig. 7**B** further emphasizes the superior electrochemical performance of the heterostructure composite compared to its individual components.

3.10.3. *Effect of electrode loading*

To further optimize electrode performance, the influence of the loading amount of ZnS:SnS_2/Bi_2S_3/GCE nanocomposite on the GCE surface was examined by varying the drop-cast volume from 2 to 8 µL Fig. 7**C**. The peak current increased progressively up to 6 µL, attributed to the formation of a uniform, thin, and conductive coating that enhanced surface coverage and facilitated analyte diffusion. Beyond 6 µL, the current slightly decreased, possibly due to thicker film formation, which restricted mass transport and increased charge diffusion resistance. Therefore, 6 µL was optimized as the ideal loading, offering maximum active sites while maintaining high conductivity and mechanical stability. The bar chart in the Fig. 7**D** supports this result, showing a clear increase in current at 6 µL, followed by a decrease at

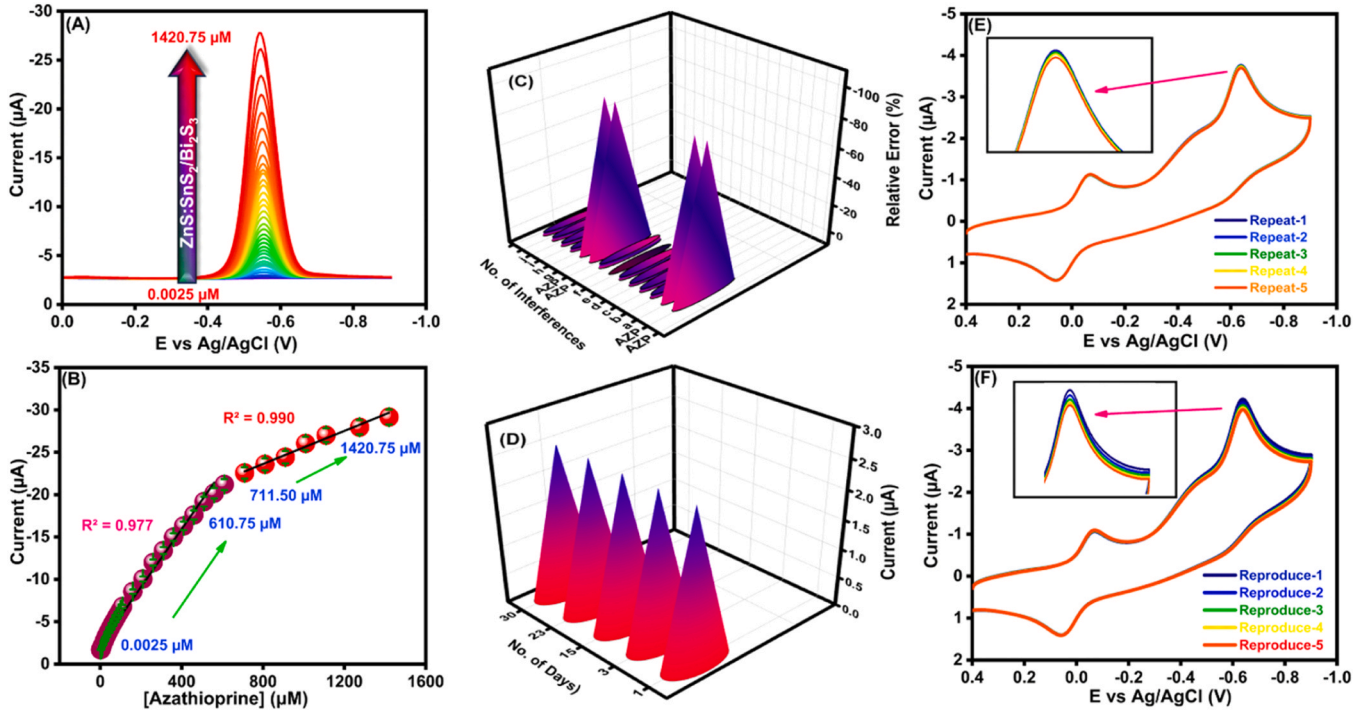

Fig. 9. (A) DPV responses of the ZnS:SnS_2/Bi_2S_3/GCE toward increasing concentrations of azathioprine (0.0025–1420.75 µM) in 0.1 M PBS (pH 7.0), showing a steady rise in cathodic current with concentration. (B) Corresponding calibration plot illustrating two distinct linear ranges $R^2 = 0.977$ and 0.990 with excellent sensitivity. (C) Selectivity evaluation of ZnS:SnS_2/Bi_2S_3/GCE toward AZA in the presence of common interferents (D) Long-term stability assessment demonstrating over 96% current retention after 30 days. (E) Repeatability test using a single modified electrode for five successive runs. (F) Reproducibility test across five independently prepared electrodes, exhibiting minimal variation and excellent fabrication uniformity.

higher volumes. This highlights how important it is to control the thickness of the film when designing effective sensors.

3.10.4. Effect of pH on electrochemical response

The effect of solution pH on the electrochemical behavior of AZA was examined over a pH range of 3–11 Fig. 7**E.** The reduction peak current gradually increased with increasing pH and reached its maximum at pH 7, after which a noticeable decline was observed under more alkaline conditions. This behavior is consistent with a proton-coupled electron-transfer (PCET) mechanism, indicating that proton availability plays a critical role in facilitating the reduction of AZA at the electrode surface. At acidic pH, excess protons hinder effective interaction between AZA and the electrode surface, while at alkaline pH, deprotonation weakens adsorption and induces electrostatic repulsion. At near neutral pH, the equilibrium between proton concentration and charge transfer is ideal allowing stable hydrogen bonding and π–π stacking interactions between AZA and the chalcogenide surface. The pH 7 environment thus provides ideal conditions for proton availability, efficient carrier mobility, and analyte binding at the ZnS:SnS_2/Bi_2S_3/GCE interface. The enhanced interaction between the S-rich surface and AZA's thio-imidazole group promotes rapid charge delocalization, facilitating reversible reduction–oxidation transitions. This balance maximizes electron transfer kinetics and signal intensity, as illustrated in Fig. 7**F**, confirming pH 7 as the optimal condition for reliable, stable, and high-sensitivity AZA detection.

3.11. Analytical performance of ZnS:SnS_2/Bi_2S_3/GCE toward AZA detection

3.11.1. Effect of analyte concentration

To evaluate the quantitative sensing performance of the ZnS:SnS_2/Bi_2S_3/GCE toward AZA, cyclic voltammetry was conducted in 0.1 M PBS (pH 7.0) with varying AZA concentrations from 50 µM to 500 µM at a fixed scan rate of 50 mV s^{-1}. As shown in Fig. 8**A**, the cathodic peak current (I_pc) increased progressively with rising AZA concentration without significant potential shifting, suggesting rapid and stable electron transfer between the analyte and the electrode surface. The strong linear relationship between I_pc and AZA concentration Fig. 8**B**, $R^2 = 0.997$ confirms highly sensitive and quantitative electrochemical behavior. This enhanced current response can be attributed to the heterojunction architecture of ZnS:SnS_2/Bi_2S_3, which provides abundant adsorption sites and promotes efficient charge separation across the S–Bi–Zn lattice. The S^{2-} rich surface facilitates strong coordination with the thiol (–SH) and imidazole nitrogen atoms of AZA, forming transient S–N and Bi–N bonding interactions that accelerate electron delocalization. Meanwhile, the narrow band-gap interface between ZnS:SnS_2 and Bi_2S_3 creates a band alignment, enabling directional electron migration from the conduction band of ZnS:SnS_2 to Bi_2S_3, minimizing recombination and improving electro-reduction efficiency.

3.11.2. Effect of analyte scan rate

The redox kinetics of AZA at the ZnS:SnS_2/Bi_2S_3/GCE were further explored through CV at scan rates ranging from 0.02 to 0.3 V·s^{-1} Fig. 8**C.** A gradual and proportional increase in both anodic and cathodic peak currents was observed with rising scan rate, indicating improved charge transfer and electron mobility across the heterostructure. At lower scan rates (0.02–0.06 V·s^{-1}, the redox peaks were well-defined and symmetric, confirming a stable diffusion-controlled process governed by the adsorption of AZA molecules on the S-enriched surface. As the scan rate increased beyond 0.1 V·s^{-1}, the cathodic peak slightly shifted toward more negative potentials, suggesting a transition to a quasi-irreversible electron-transfer regime, where kinetic limitations and partial charge accumulation at the interface begin to influence electron flow. The linear correlation between peak current (I_pc) and the square root of the scan rate $R^2 = 0.993$, Fig. 7**D** verifies that diffusion dominates the overall process, while the slope and intercept reflect the strong electron

coupling and high diffusion coefficient of AZA on the ZnS:SnS_2/Bi_2S_3/GCE surface. The enhanced electrochemical performance of the ZnS:SnS_2/Bi_2S_3 heterostructure can be attributed to the formation of a Type-II heterojunction among the coupled sulfide domains. Based on literature-reported band-edge positions of ZnS, SnS_2, and Bi_2S_3, the staggered energy alignment is expected to facilitate directional charge migration across the interfaces, thereby accelerating interfacial electron transport and reducing charge recombination. This interfacial interaction is consistent with the lower charge-transfer resistance observed from EIS analysis and the enhanced redox response obtained in CV and DPV measurements. Moreover, the intimate heterointerfacial contact confirmed by TEM, EDS mapping, and XPS analyses further supports efficient electronic communication between the constituent sulfides [30].

3.12. Differential pulse voltammetry sensing performance, selectivity, operational stability, and reproducibility

3.12.1. Differential pulse voltammetry (DPV)

The electrochemical detection capability of the ZnS:SnS_2/Bi_2S_3/GCE toward AZA was investigated using DPV in 0.1 M PBS (pH 7.0). As shown in Fig. 9**A**, a systematic increase in cathodic peak current was observed with increasing AZA concentration (0.0025 μM – 1420 μM), indicating efficient electron exchange and stable adsorption on the heterostructured surface. The absence of potential shifts or peak broadening confirms the high stability of the interface and the fast redox kinetics enabled by the coupled semiconductor junction. The calibration plot Fig. 9**B** shows two distinct linear ranges with regression coefficients of $R^2 = 0.977$ (0.0025–610.25 μM) and $R^2 = 0.990$ (711.50–1420.75 μM), demonstrating wide dynamic linearity. The appearance of two linear ranges can be attributed to different AZA interaction regimes at the ZnS:SnS_2/Bi_2S_3/GCE interface. In the lower concentration region, abundant accessible active sites and open porous channels allow efficient AZA adsorption and rapid charge transfer, resulting in a strong linear current response. At higher AZA concentrations, partial occupation of active sites and increased diffusion resistance reduce the rate of interfacial electron transfer, producing a second linear range with a different sensitivity. Therefore, the dual linear behavior is mainly associated with concentration-dependent adsorption and surface saturation effects rather than instability of the sensing platform. The detection limit (LOD), from $3\sigma/s$, was 0.0012 μM, and the sensitivity calculated using **equation−1** [50] 0.52 μA μM^{-1} cm^{-2}. The enhanced DPV response toward AZA originates from the interfacial interaction among ZnS, SnS_2, and Bi_2S_3, which promotes rapid charge migration and improves adsorption of AZA molecules onto the hierarchically porous electrode surface. The coupled sulfide framework provides abundant electroactive sites and facilitates proton-coupled electron transfer during the reduction of AZA, resulting in amplified current response and improved sensing sensitivity.

$$\boldsymbol{LOD} = (\mathbf{3} \times \boldsymbol{SD} - \boldsymbol{s}) \quad (1)$$

3.12.2. Selectivity and interference evaluation

To verify the selectivity of the developed sensor, DPV responses were recorded in the presence of possible interfering species such as a-K^+, b-Na^+, c-Fe^{3+}, D-uric acid, e-glucose, f-nitrophenol, g – Ascorbic acid h-metronidazole-and i-dimetridazole. As shown in Fig. 9**C**, the AZA peak remained unaffected, with negligible signal variation even at interferent concentrations 10–50 times higher. The relative error stayed below 2%, confirming the excellent anti-interference property of the heterostructured surface. This high selectivity arises from the π–π and hydrogen-bond interactions between AZA and the S/Bi lattice, which favor the target analyte over electrochemically similar species. The influence of common coexisting species, including metal ions and electroactive biomolecules, on the AZA sensing response was further examined to evaluate selectivity. Even in the presence of excess concentrations of interfering compounds such as glucose, uric acid, dopamine, ascorbic acid, metronidazole, and dimetridazole, the variation in the AZA current response remained within ±5%, indicating excellent anti-interference performance and high sensing specificity of the ZnS:SnS_2/Bi_2S_3-modified electrode.

Table 3
Summary of the analytical performance of previously reported electrochemical sensors for AZA determination, presented for comparison with the current work.

S. No	Electrode	Method	Linear range (μM)	LOD (μM)	Ref.
1	Mn_2O_3/rGO on SPCE	DPV	0.009 – 573.5	0.004	[51]
2	NDG/CS modified GCE	CV	0.2 – 100	0.065	[52]
3	$AgBiS_2$/AGr on GCE	it	2.54–17.4	0.007	[53]
4	SiO_x/C–GA on SPCE	DPV	0.02 – 415	0.002	[54]
5	SnS_2/C modified GCE	DPV	0.001–12750	0.005	[55]
6	NNO/rGO on GCE	DPV	0.4–693	0.003	[56]
7	EuO/g-CN on GCE	DPV	0.02–427	0.008	[57]
8	**ZnS:SnS_2/Bi_2S_3/GCE**	**DPV**	**0.0025–1420.75**	**0.0012**	**This Work**

3.12.3. Operational stability and long-term durability

The long-term operational stability of the ZnS:SnS_2/Bi_2S_3/GCE was carefully evaluated over a 30-day period Fig. 9**D**. The electrode retained over 96% of its initial current response, demonstrating outstanding structural robustness and chemical durability of the heterostructured surface. This remarkable stability can be attributed to the strong interfacial bonding between ZnS:SnS_2 and Bi_2S_3 layers, which prevents structural delamination and suppresses surface oxidation during repeated redox cycling. Furthermore, the presence of abundant S^{2-} and Bi^{3+} sites enhances charge retention and minimizes potential drift by maintaining a uniform electron density at the electrode–electrolyte interface.

The repeatability test Fig. 9**E**, carried out using a single electrode for five consecutive measurements under identical conditions, yielded a relative standard deviation (RSD) of 0.24%, indicating exceptional signal reproducibility and minimal electrode fouling. This consistency highlights the robust anchoring of the composite layer on the GCE surface and its strong adhesion against electrochemical stress. Similarly, reproducibility was evaluated across five independently prepared ZnS:SnS_2/Bi_2S_3/GCE modified electrodes Fig. 9**F**, showing an RSD of 0.31%. The very low variation among electrodes confirms the high uniformity of the synthesis and coating process, excellent dispersion of the nanostructures, and consistent active site exposure. The repeatability and reproducibility analyses of the ZnS:SnS_2/Bi_2S_3/GCE were further evaluated through consecutive electrochemical measurements, and the corresponding original data and error-bar analysis are provided in Supplementary Fig. S3.All electrochemical measurements were performed in triplicate (n = 3), and the reported values represent the mean response with corresponding RSD. Repeatability was evaluated using repeated measurements with the same modified electrode, while reproducibility was assessed using independently fabricated electrodes under identical experimental conditions. Table 3 presents a comparison of previous electrochemical sensors for the detection of AZA. Compared with previously reported sulfide-based AZA sensing platforms such as SnS_2/C/GCE and $AgBiS_2$/AGr/GCE, the developed ZnS:SnS_2/Bi_2S_3 heterostructure exhibited a broader linear detection range and lower detection limit together with improved operational stability. The enhanced sensing performance can be attributed to the hierarchically porous heterointerface, which facilitates efficient electrolyte penetration, rapid analyte diffusion, and improved interfacial charge-transfer

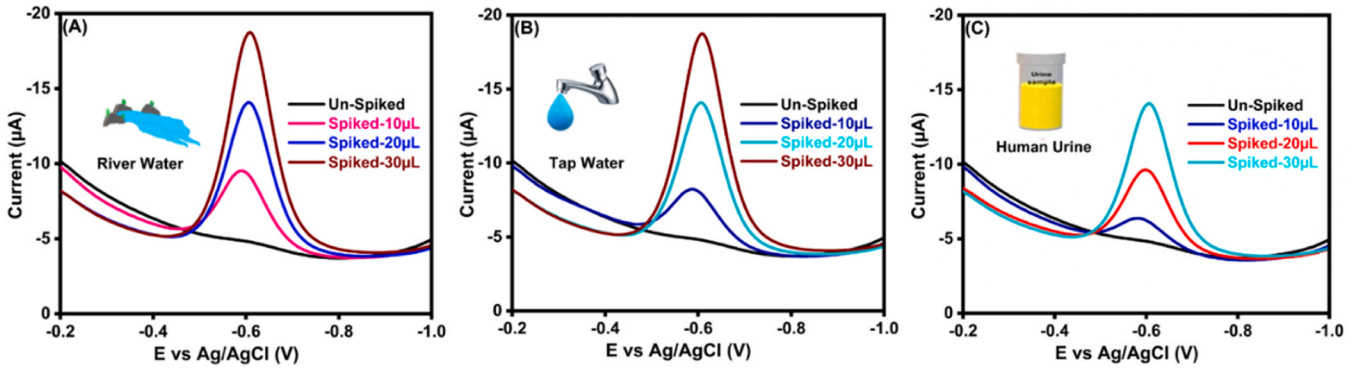

Fig. 10. (A–C) DPV responses of the ZnS:SnS_2/Bi_2S_3/GCE for un-spiked and AZA-spiked real samples, including (A) river water, (B) tap water, and (C) human urine. Un-spiked samples show negligible background signals, while spiked samples exhibit distinct cathodic peaks with increasing current proportional to AZA concentration, confirming efficient detection even in complex matrices.

behavior. Furthermore, the coupled ZnS, SnS_2, and Bi_2S_3 domains provide abundant electroactive sites and accessible adsorption pathways, contributing to the amplified electrochemical response toward AZA detection.

3.13. Real sample analysis

3.13.1. Sample preparation and evaluation

To validate the practical feasibility and robustness of the ZnS:SnS_2/Bi_2S_3/GCE sensor for AZA detection, real-sample recovery studies were carried out using river water, tap water, and human urine as representative matrices Fig. 10 **A–C.** This evaluation provides insight into the sensor capability to operate under realistic environmental and biological conditions where ionic strength, organic residues, and pH fluctuations could interfere with electrochemical performance. River and tap water samples were freshly collected from the Nanzi River and laboratory water supply (Taipei, Taiwan). Both were passed through a 0.22 μm syringe filter to eliminate suspended solids and used without pH modification to emulate natural environmental states. For recovery testing, known concentrations of AZA (10, 20, and 30 μL) were spiked into each sample, while un-spiked aliquots served as negative controls. Human urine samples were obtained from healthy adult volunteers, filtered through a 0.22 μm membranes and diluted fivefold with phosphate buffer (0.1 M, pH 7.0) to minimize matrix viscosity and protein interference before spiking with the same AZA concentrations.

DPV responses for un-spiked samples exhibited negligible background currents, confirming the absence of interfering electroactive species within the native matrices. After AZA addition, distinct cathodic peaks emerged with progressively increasing current intensity proportional to the spiked concentration Fig. 10**A–C.** This trend demonstrates the excellent selectivity, sensitivity, and anti-fouling behaviour of the heterostructure ZnS:SnS_2/Bi_2S_3/GCE interface, which enables efficient electron transfer and stable redox interaction even in complex sample environments.

Real-sample validation is a crucial step for translating laboratory-based sensors into real-world applications. It reveals the sensor's matrix tolerance, stability under ionic competition, and resistance to organic contamination parameters that directly influence field performance. The superior response observed in all three matrices arises from the coupling between ZnS:SnS_2 and Bi_2S_3 which facilitates rapid charge transfer through built-in heterojunctions, while sulfur-rich surfaces enhance AZA adsorption via π–π stacking and N–H-S hydrogen bonding. Moreover, the layered nanostructure maintains accessible active sites, promoting efficient diffusion of AZA molecules even within complex biological fluids. Table S1 show the recoveries obtained for river water, tap water, and human urine were 97.6–101.2%, with RSD below 2.5%, confirming both precision and reliability. These results affirm that the ZnS:SnS_2/Bi_2S_3 sensor demonstrates excellent applicability for monitoring pharmaceutical residues in environmental water systems, highlighting its potential as a reliable platform for the detection of emerging drug contaminants and supporting environmental pollution surveillance.

4. Conclusion

In this work, ZnS:SnS_2/Bi_2S_3 heterostructured composite was successfully fabricated through a combined hydrothermal and ultrasonication-assisted method and employed as an efficient electrochemical sensing platform for AZA detection. Structural and surface characterization confirmed the successful formation of the heterostructure with strong interfacial interactions, hierarchical morphology, and abundant electroactive sites. The fabricated ZnS:SnS_2/Bi_2S_3 /GCE exhibited significantly enhanced electrochemical performance, including fast electron transfer, wide linear detection ranges (0.0025–610.25 and 711.50–1420.75 μM), and a low detection limit of 0.0012 μM. The improved sensing performance was mainly attributed to the heterojunction effect and hierarchically porous architecture, which facilitated efficient charge transport and analyte diffusion. Furthermore, the sensor demonstrated satisfactory stability and excellent recovery toward AZA detection in real water and urine samples, confirming its practical applicability. Overall, the present study provides a promising strategy for designing high-performance electrochemical sensing platforms for pharmaceutical and environmental monitoring applications.

CRediT authorship contribution statement

Shih-Hsuan Chen: Software, Formal analysis, Data curation. **Neeraja Bose:** Writing – review & editing, Validation. **Kumar Gokulkumar:** Writing – review & editing, Writing – original draft, Software, Methodology. **Kun-Mu Lee:** Writing – review & editing, Supervision, Resources, Project administration, Investigation, Funding acquisition, Formal analysis, Data curation, Conceptualization. **Barani Kumar Duvaragan:** Software. **Sakthivel Kogularasu:** Software, Resources, Data curation.

Declaration of Competing Interest

The authors declare that they have no known competing financial interests or personal relationships that could have appeared to influence the work reported in this paper.

Acknowledgment

The authors gratefully acknowledge financial support from the National Science and Technology Council (NSTC), Taiwan, under Project No. NSTC 111–2223-E−182–001-MY4. This research was also

supported by the Chang Gung University, Taiwan. Project No (URRPD2R0011).

Appendix A. Supporting information

Supplementary data associated with this article can be found in the online version at doi:10.1016/j.jece.2026.123587.

Data availability

Data will be made available on request.

References

[1] S.J. Meggitt, J.C. Gray, N.J. Reynolds, Azathioprine dosed by thiopurine methyltransferase activity for moderate-to-severe atopic eczema: a double-blind, randomised controlled trial, Lancet 367 (9513) (2006) 839–846.
[2] A. Fraser, T. Orchard, D. Jewell, The efficacy of azathioprine for the treatment of inflammatory bowel disease: a 30 year review, Gut 50 (4) (2002) 485–489.
[3] P. Yudkin, et al., Overview of azathioprine treatment in multiple sclerosis, Lancet 338 (8774) (1991) 1051–1055.
[4] D. McGovern, et al., Azathioprine intolerance in patients with IBD may be imidazole-related and is independent of TPMT activity, Gastroenterology 122 (3) (2002) 838–839.
[5] G.G. BHW Lamers, R.A. van Hogezand, R.A. Veenendaal, C, Azathioprine: an update on clinical efficacy and safety in inflammatory bowel disease, Scand. J. Gastroenterol. 34 (230) (1999) 111–115.
[6] D. McGovern, D. Jewell, Risks and benefits of azathioprine therapy, Gut 54 (8) (2005) 1055–1059.
[7] B. Pasternak, et al., Use of azathioprine and the risk of cancer in inflammatory bowel disease, Am. J. Epidemiol. 177 (11) (2013) 1296–1305.
[8] W.R. Connell, et al., Long-term neoplasia risk after azathioprine treatment in inflammatory bowel disease, Lancet 343 (8908) (1994) 1249–1252.
[9] C. Li, et al., Towards practical and sustainable SERS: a review of recent developments in the construction of multifunctional enhancing substrates, J. Mater. Chem. C. 9 (35) (2021) 11517–11552.
[10] P. Giraudeau, Challenges and perspectives in quantitative NMR, Magn. Reson. Chem. 55 (1) (2017) 61–69.
[11] C. Dodeigne, L. Thunus, R. Lejeune, Chemiluminescence as diagnostic tool. A review, Talanta 51 (3) (2000) 415–439.
[12] M. Swartz, HPLC detectors: a brief review, J. Liq. Chromatogr. Relat. Technol. 33 (9-12) (2010) 1130–1150.
[13] K. Gokulkumar, I.J.D. Priscillal, S.-F. Wang, Deep eutectic solvent-mediated synthesis of PDA coated f-CNF doped ZnS nanoparticles for electrode modification: Innovative sensing platform for determination of pollutant 3-nitrophenol, J. Alloy. Compd. 924 (2022) 166561.
[14] K. Gokulkumar, et al., Nanoparticles of SnS on carbon nanofibers for electrochemical detection of vanillin, ACS Appl. Nano Mater. 7 (11) (2024) 13183–13193.
[15] K. Gokulkumar, et al., Enhanced electrochemical detection of tartrazine in beverages and liquid soap via nickel phosphide-adorned functionalized carbon nanofibers, J. Taiwan. Inst. Chem. Eng. 157 (2024) 105420.
[16] P. Manimaran, et al., Ni-Metal–Organic Framework/β-Cyclodextrin/Functionalized Carbon Black Nanomaterials for Enhanced Electrochemical Sensing of Metronidazole in Environmental and Clinical Samples, ACS Appl. Nano Mater. (2025).
[17] K. Gokulkumar, et al., Enhanced electrochemical detection of the antibiotic levofloxacin using temperature optimized Er2MoO6 nanomaterials for environmental monitoring, J. Water Process. Eng. 78 (2025) 108757.
[18] B. Sriram, et al., Facile hydrothermal synthesis and electrocatalytic activity of rods-like silver tungstate decorated graphitic carbon nitride nanocomposite: A selective electrochemical detection of theobromine, Chem. Eng. J. (2025) 165397.
[19] B. Sriram, et al., Scheelite-type rare earth vanadates TVO4 (T= Ho, Y, Dy) electrocatalysts: Investigation and comparison of T site variations towards bifunctional electrochemical sensing application, Chem. Eng. J. 451 (2023) 138694.
[20] J. Ni, et al., Bismuth chalcogenide compounds Bi2× 3 (X= O, S, Se): Applications in electrochemical energy storage, Nano Energy 34 (2017) 356–366.
[21] Y. Zhang, et al., Nanostructured metal chalcogenides for energy storage and electrocatalysis, Adv. Funct. Mater. 27 (35) (2017) 1702317.
[22] S. Palchoudhury, et al., Transition metal chalcogenides for next-generation energy storage, Nanoscale Adv. 5 (10) (2023) 2724–2742.
[23] H. Liu, et al., Hollow cubic ZnS-SnS2 heterostructures as sulfur hosts to enhance chemisorption and catalytic conversion of polysulfides for lithium sulfur batteries, J. Electroanal. Chem. 932 (2023) 117252.
[24] L. Cao, et al., Synergistical coupling interconnected ZnS/SnS2 nanoboxes with polypyrrole-derived N/S dual-doped carbon for boosting high-performance sodium storage, Small 15 (9) (2019) 1804861.
[25] Z. Jiao, et al., Combining crystal planes and heterojunctions of ZnS/SnS2 boosts photocatalytic performance, J. Chem. Phys. 162 (5) (2025).
[26] J. Deng, et al., Hollow ZnS-SnS2@ MoS2 heterostructures for high-efficiency adsorption-storage-catalysis of polysulfides in lithium-sulfur batteries, J. Alloy. Compd. 1010 (2025) 177172.
[27] W. Yao, et al., ZnS-SnS@ NC heterostructure as robust lithiophilicity and sulfiphilicity mediator toward high-rate and long-life lithium–sulfur batteries, ACS nano 15 (4) (2021) 7114–7130.
[28] S. Vadivel, et al., Facile large scale synthesis of Bi2S3 nano rods–graphene composite for photocatalytic photoelectrochemical and supercapacitor application, Appl. Surf. Sci. 351 (2015) 635–645.
[29] S.-J. Huang, et al., Synthesis and characterization of Bi2S3-embedded carbon nanofibers as a novel electrochemical biosensor for the detection of mycotoxin zearalenone in food crops, FlatChem 45 (2024) 100652.
[30] S. Paul, et al., 3D/2D Bi 2 S 3/SnS 2 heterostructures: superior charge separation and enhanced solar light-driven photocatalytic performance, CrystEngComm 23 (11) (2021) 2276–2288.
[31] L. Zheng, et al., Photo/electrochemical applications of metal sulfide/TiO2 heterostructures, Adv. Energy Mater. 10 (1) (2020) 1902355.
[32] X. Chen, et al., Two-dimensional ZnS/SnS2 heterojunction as a direct Z-scheme photocatalyst for overall water splitting: a DFT study, Materials 15 (11) (2022) 3786.
[33] S. Kausar, et al., Mesoporous Materials: Synthesis and electrochemical applications, Electrochem. Commun. 169 (2024) 107836.
[34] R.K. Mishra, K. Verma, Defect engineering in nanomaterials: Impact, challenges, and applications, Smart Mater. Manuf. (2) (2024) 100052.
[35] F.P.D. Disouza, et al., Synergetic effect of ZnS: SnS2/reduced graphene oxide heterostructures for electrochemical detection of carcinogenic pollutant Maleic hydrazide, Microchem. J. 193 (2023) 109087.
[36] S. Dong, et al., Bismuth based nanoflower shaped heterojunction with enhancing electrocatalytic activity for nitrite sensing, Sens. Actuators B Chem. (2025) 139165.
[37] S. Dong, et al., Assembling of self-supported metal− organic framework aerogel heterojunction for enhancing glucose sensing, J. Environ. Chem. Eng. 13 (2) (2025) 116041.
[38] S. Dong, et al., Facile and efficient synthesis of sweater-ball shaped metal-organic framework/nickel sulfide nanoheterojunction for boosting electrochemical glucose sensing, Talanta 275 (2024) 126129.
[39] K. Shen, et al., Recent progress in binder-free electrodes synthesis for electrochemical energy storage application, Batter. & Supercaps 4 (6) (2021) 860–880.
[40] Z.M. Fard, et al., Efficient visible light-driven core–shell-structured ZnS@ Ag 2 S nanoparticles-anchored reduced graphene oxide for the reduction of Cr (vi), New. J. Chem. 44 (34) (2020) 14670–14678.
[41] D.G. Buldu, et al., Influence of sulfurization temperature on Cu2ZnSnS4 absorber layer on flexible titanium substrates for thin film solar cells, Phys. Scr. 93 (2) (2018) 024002.
[42] Y. Zhao, et al., Phonons in Bi 2 S 3 nanostructures: Raman scattering and first-principles studies, Phys. Rev. BCondens. Matter Mater. Phys. 84 (20) (2011) 205330.
[43] A. Fairbrother, et al., ZnS grain size effects on near-resonant Raman scattering: optical non-destructive grain size estimation, CrystEngComm 16 (20) (2014) 4120–4125.
[44] S. Sohila, et al., Optical and Raman scattering studies on SnS nanoparticles, J. Alloy. Compd. 509 (19) (2011) 5843–5847.
[45] T.J. Whittles, et al., Band alignments, valence bands, and core levels in the tin sulfides SnS, SnS2, and Sn2S3: experiment and theory, Chem. Mater. 28 (11) (2016) 3718–3726.
[46] J. Xu, et al., Preparation of ZnS nanoparticles by ultrasonic radiation method, Appl. Phys. A 66 (6) (1998) 639–641.
[47] J. Morales-Rodríguez, et al., Facile synthesis of the Bi2S3@ rGO composite via chemical precipitation for potential applications in electrochemical energy storage, J. Energy Storage 125 (2025) 116948.
[48] B. Sriram, et al., Deep eutectic solvent-mediated synthesis of spinel zinc chromite nanoparticles: a simple label-free electrochemical sensor for dopamine and ascorbic acid, ACS Appl. Nano Mater. 6 (19) (2023) 17593–17602.
[49] J. Anupriya, et al., Enhanced electrochemical performance of in-situ synthesized Cu nanoparticle/C spheres composite for highly sensitive sensing of azathioprine immunosuppressive drug, Composites Part B Engineering 242 (2022) 110079.
[50] K. Gokulkumar, et al., Zinc molybdate/functionalized carbon nanofiber composites modified electrodes for high-performance amperometric detection of hazardous drug Sulfadiazine, OpenNano 10 (2023) 100131.
[51] S.V. Selvi, et al., An electrochemical platform for the selective detection of azathioprine utilizing a screen-printed carbon electrode modified with manganese oxide/reduced graphene oxide, New. J. Chem. 45 (7) (2021) 3640–3651.
[52] S. Shahrokhian, M. Ghalkhani, Glassy carbon electrodes modified with a film of nanodiamond–graphite/chitosan: application to the highly sensitive electrochemical determination of Azathioprine, Electrochim. Acta 55 (11) (2010) 3621–3627.
[53] K. Alagumalai, et al., AgBiS2 embedded activated graphene nanolayer for sensing azathioprine in biospecimens, Colloids Surf. A Physicochem. Eng. Asp. 685 (2024) 133243.
[54] B. Mutharani, et al., Devising a universal tailored monomer molecular strategy for SiOx/carbon hollow spheres as a synergistic electrocatalyst in azathioprine sensing, Mater. Today Chem. 26 (2022) 101058.
[55] S.P. Sivaji, et al., Promote the electrocatalytic activity through the assembly of hexagonal SnS2/C sphere nanocomposite for determination of the

immunosuppressant drug azathioprine in biological samples, Colloids Surf. A Physicochem. Eng. Asp. 667 (2023) 131335.
[56] R. Pandiyan, P. Rameshkumar, S.-M. Chen, Hydrothermal synthesis of pure phase doughnut-like NiNb2O6 nanostructures decorated reduced graphene oxide for sensitive electrochemical detection of azathioprine in water samples, Process. Saf. Environ. Prot. (2025) 107446.
[57] B. Karuppaiah, et al., Europium oxide decorated on graphitic carbon nitride as electrochemical sensor for ultra-selective enhanced electrocatalytic detection of azathioprine, Int. J. Electrochem. Sci. 17 (4) (2022) 220434.